CrossMark

Interaction of a Relativistic Magnetized Collisionless Shock with a Dense Clump

Sara Tomita[1,2] , Yutaka Ohira[3] , Shigeo S. Kimura[1,2] , Kengo Tomida[2] , and Kenji Toma[1,2]
[1] Frontier Research Institute for Interdisciplinary Sciences, Tohoku University, Sendai, 980-8578, Japan; tomisara@astr.tohoku.ac.jp
[2] Astronomical Institute, Graduate School of Science, Tohoku University, Sendai, 980-8578, Japan
[3] Department of Earth and Planetary Science, The University of Tokyo, 7-3-1 Hongo, Bunkyo-ku, Tokyo, 113-0033, Japan

Abstract

The interactions between a relativistic magnetized collisionless shock and dense clumps have been expected to play a crucial role in magnetic field amplification and cosmic-ray acceleration. We investigate this process using two-dimensional Particle-In-Cell (PIC) simulations, for the first time, where the clump size is much larger than the gyroradius of the downstream particles. We also perform relativistic magnetohydrodynamic (MHD) simulations for the same condition, to see the kinetic effects. We find that particles escape from the shocked clump along magnetic field lines in the PIC simulations, so that the vorticity is lower than that in the MHD simulations. Moreover, in both the PIC and MHD simulations, the shocked clump quickly decelerates because of relativistic effects. Owing to the escape and the deceleration, the shocked clump cannot amplify the downstream magnetic field in relativistic collisionless shocks. This large-scale PIC simulation opens a new window to understanding large-scale behaviors in collisionless plasma systems.

Unified Astronomy Thesaurus concepts: High energy astrophysics (739); Magnetohydrodynamics (1964); Shocks (2086); Plasma physics (2089); Laboratory astrophysics (2004)

1. Introduction

Relativistic shocks are formed in high-energy astrophysical phenomena such as gamma-ray bursts, relativistic jets from active galactic nuclei, and pulsar wind nebulae. In high-temperature astrophysical plasmas, shocks are often collisionless, in the sense that Coulomb interactions do not play an important role in the shock dissipation. Instead, shocks are mediated by the collective motion of charged particles, which generates the fluctuation of the electromagnetic fields, disturbing particle orbits. In addition, some particles are accelerated to very large energies compared with the downstream temperature in the collisionless shock (Spitkovsky 2008a; Sironi et al. 2013). Therefore, the collisionless shock is believed to accelerate cosmic rays and emit powerful nonthermal radiations, and is expected to have a crucial role in various high-energy astrophysical phenomena (Kotera & Olinto 2011; Tanaka & Takahara 2011; Fang et al. 2012; Murase et al. 2012; Kakuwa et al. 2015; Kimura et al. 2018; Zhang et al. 2018; Heinze et al. 2020).

The magnetic field is expected to be amplified in the collisionless shock, to enhance the acceleration rate and radiation efficiency of accelerated electrons (e.g., Uchiyama et al. 2007; MAGIC Collaboration et al. 2019a, 2019b; Lhaaso Collaboration et al. 2021; Breuhaus et al. 2022). For example, afterglow observations of gamma-ray bursts suggest that the downstream magnetic field is much larger than the shock compressed value (Santana et al. 2014; Abdalla et al. 2019; Tomita et al. 2019, and references therein). In collisionless shocks, kinetic plasma instabilities are induced, amplifying the magnetic field (Weibel 1959; Lucek & Bell 2000; Ohira et al. 2009). In relativistic collisionless shocks, the Weibel instability rapidly generates the strong magnetic field fluctuation

(Weibel 1959; Kato 2005), whose characteristic wavelength is the plasma skin depth, and much smaller than the astrophysical scale. Although the Weibel instability is required for particle acceleration in the relativistic shock (Niemiec et al. 2006), such a small-scale magnetic field rapidly decays near the shock front (Spitkovsky 2008b). Therefore, in addition to the Weibel instability, another amplification mechanism of the magnetic field is required (Keshet et al. 2009; Tomita & Ohira 2016; Tomita et al. 2019).

Shock waves generally propagate into inhomogeneous media. For example, the interaction of shock waves with a dense clump has been investigated by hydrodynamical simulations and laboratory experiments for a long time (Stone & Norman 1992; Atzeni & Meyer-ter-Vehn 2004; Inoue et al. 2009; Nishihara et al. 2010; Sano et al. 2013; Perkins et al. 2017; Hennebelle & Inutsuka 2019; Sano et al. 2021; Zhou et al. 2021). Past studies show that in magnetized plasmas with a sufficiently large conductivity, the shock–clump interactions generate turbulence that amplifies the magnetic fields. The turbulent dynamo in the shock's downstream region is expected to play a crucial role in the magnetic field amplification, cosmic-ray acceleration, and enhancement of nonthermal radiation in many astrophysical objects (Giacalone & Jokipii 2007; Sironi & Goodman 2007; Inoue et al. 2011; Mizuno et al. 2011; Fraschetti 2013; Mizuno et al. 2014). Recently, the physical processes of collisionless shocks have been actively investigated by Particle-In-Cell (PIC) simulations (Spitkovsky 2008a, 2008b; Niemiec et al. 2012; Matsumoto et al. 2013; Iwamoto et al. 2019), but the upstream medium has usually been assumed to be uniform. Although there are a few exceptional studies (Sironi & Spitkovsky 2012; Tomita & Ohira 2016; Tomita et al. 2019), the upstream inhomogeneity has been assumed to be a simple structure like a plane wave.

Since the mean free path of Coulomb collision is longer than the system size in collisionless shocks, particles can easily escape from the dense clump by diffusion and free-streaming motion along a magnetic field line. After the dense clump

passes through the collisionless shock front, the thermal velocity in the clump becomes high, so that particles in the clump would escape in the sound crossing time (Tomita & Ohira 2016). However, this escape process has not been taken into account in the early studies of the shock–clump interaction using magnetohydrodynamic (MHD) simulations (Shin et al. 2008; Inoue et al. 2011; Mizuno et al. 2011; Sano et al. 2013; Mizuno et al. 2014). Therefore, it is an open problem as to whether or not the shock–clump interaction in collisionless plasmas can amplify the downstream magnetic field by the turbulent dynamo. In this Letter, we present the first ab initio PIC simulation of the shock–clump interaction in collisionless plasmas, and perform MHD simulations for the same conditions, to see the kinetic effects.

2. Simulation Setup

We perform fully kinetic two-dimensional simulations of relativistic shocks propagating into inhomogeneous media using an electromagnetic PIC code (Matsumoto et al. 2013; Ikeya & Matsumoto 2015; Matsumoto et al. 2015). The simulation frame and box are set in the downstream rest frame and the $x - y$ plane. In this PIC simulation, particles are continuously injected, with a drift velocity in the x-direction from one side of the simulation boundary, and reflected on the opposite side. We apply a moving injection boundary to reduce the computational costs and the numerical heating by numerical Cherenkov instability (Godfrey 1974). A periodic boundary condition is assumed in the y-direction. The initial upstream density distribution in the simulation frame is given by

$$n(x, y) = \begin{cases} n_0 & (r > 2R_{\rm cl}) \\ n_0 + (n_{\rm cl} - n_0)\left\{1 + \cos\left(\dfrac{\pi r}{2R_{\rm cl}}\right)\right\} & (r \leqq 2R_{\rm cl}) \end{cases},$$
$$r \equiv \sqrt{\frac{(x - x_{\rm c})^2}{\Gamma^2} + (y - y_{\rm c})^2},$$

where n_0 and Γ are the number density in the uniform region and the bulk Lorentz factor of the upstream plasma, and $x_{\rm c}$ and $y_{\rm c}$ are the x and y coordinates at the clump center, respectively. $n_{\rm cl}$ is the number density at the half width at half maximum of the clump, $R_{\rm cl}$. Since we consider a spherical clump structure with the radius $R_{\rm cl}$ in the upstream rest frame, its structure is compressed along the x-direction, due to the Lorentz contraction in the simulation frame. The density structure is not stable, because the temperature is uniform. However, the thermal velocity in the upstream region is much smaller than the speed of light, so the density structure in our PIC simulation does not change significantly until the clump interacts with the shock front.

According to previous simulations, electrons are heated to near equipartition with ions in the downstream region for relativistic shocks (Spitkovsky 2008b; Kumar et al. 2015), so that electron–ion plasmas can be approximately treated by electron–positron plasmas. Hence, we consider electron–positron plasmas to reduce the computational costs of this study. The density, n, represents the total density of electrons and positrons. The uniform magnetic field parallel to the y-direction is imposed in the upstream region, $\boldsymbol{B} = B_0\boldsymbol{e}_y$. The magnetic field strength, B_0, is characterized by the plasma magnetization parameter, $\sigma_{\rm e} = B_0^2/(8\pi\Gamma n_0 m_{\rm e}c^2)$, where $m_{\rm e}$

and c are the electron mass and the speed of light, respectively. The simulation box size is $L_x \times L_y = 3120c/\omega_{\rm pe} \times 1200c/\omega_{\rm pe}$ at the end of simulation, $t_{\rm end} = 6300\omega_{\rm pe}^{-1}$, where $\omega_{\rm pe} = (4\pi n_0 e^2/\Gamma m_{\rm e})^{1/2}$ is the plasma frequency of the electron–positron plasma and e is the elementary charge. The cell sizes and time steps of the simulations are $\Delta x = \Delta y = 0.1c/\omega_{\rm pe}$ and $\Delta t = 0.1\omega_{\rm pe}^{-1}$, respectively.[4] The number of simulation particles is 60 in each cell of the uniform region, for electrons and positrons.

We perform several simulations with different densities of the clump, $n_{\rm cl}$, whose values are 1.5, 2.0, 4.0, 6.0, 8.0, 10.0, and 20.0, respectively. The other parameters and the thermal velocity of the upstream plasma are fixed to be $R_{\rm cl} = 300c/\omega_{\rm pe}$, $\Gamma = 10$, $\sigma_{\rm e} = 10^{-3}$, and $v_{\rm th} = 0.18c$ in this work. Then, the ratio of the clump size to the gyroradius[5] of the downstream thermal electrons and positrons is $R_{\rm cl}/r_{\rm g} = 53.7 \gg 1$. This indicates that the downstream plasma is expected to be well magnetized on the clump scale.

To clarify the effects of particle escape on the turbulent dynamo, we also perform MHD simulations for the shock–clump interaction with the open source code, Athena++ (White et al. 2016; Stone et al. 2020), where we use the relativistic HLLE Riemann solver, a second-order piecewise linear reconstruction, and a second-order Runge–Kutta time integrator. All the physical parameters are the same as those in the PIC simulations. The cell sizes and time steps of MHD simulations are $\Delta x = 0.1\Delta y = R_{\rm cl}/3000$ and $\Delta t = 0.1\Delta x/c$, respectively. The density structure in the MHD simulation is stable, because the pressure is uniform; that is, the structure is in the dynamic equilibrium state.
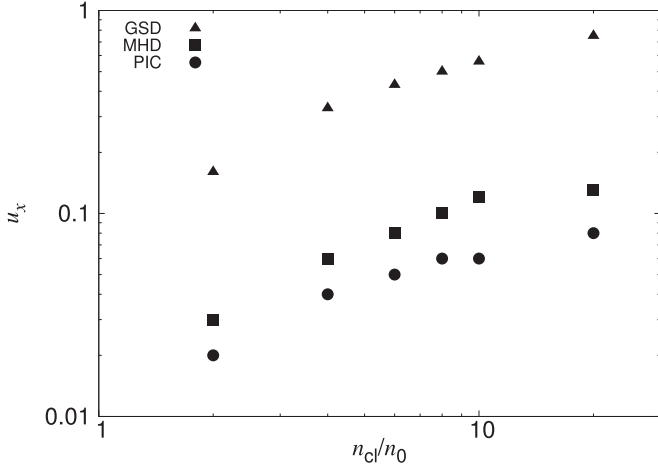
3. Results

Figure 1 shows the x component of four velocity at the high-density clump, u_x, at $t = 2t_{\rm esc}$, as a function of the density of the clump, $n_{\rm cl}/n_0$. The time, t, represents the elapsed time since the clump has interacted with the shock front. $t_{\rm esc} = R_{\rm cl}/0.5c = 600\omega_{\rm pe}^{-1}$ is the escape time along the magnetic field line (the y-direction), where the mean particle velocity along the magnetic field line is assumed to be $0.5c$. In addition to the MHD and PIC results, theoretical expectations based on the geometrical shock dynamics (GSD; Sironi & Goodman 2007) are plotted in Figure 1. The GSD approximation assumes that the downstream flow is determined by the forward-going Riemann characteristics in the isentropic and homogeneous far-downstream region. Our MHD simulations show that the clump velocities in the downstream region are much lower than those expected from the GSD approximation. Sironi & Goodman (2007) estimated the downstream velocity disturbance due to the clump–shock interaction based on the GSD approximation, without taking into account the deceleration of the shocked clump. However, we observe the significant deceleration of the shocked clump in the downstream region.

The reason for this rapid deceleration is as follows. At first, the clump decelerates due to the shock interaction in the shock transition time. After that, the shocked clump decelerates

---

[4] In order to suppress the numerical Cherenkov instability in PIC simulations (Godfrey 1974), Maxwell's equations are solved by an implicit method with the Courant–Friedrichs–Lewy number of 1.0 (Ikeya & Matsumoto 2015). Thanks to the implicit method, there are no side effects.

[5] Coincidentally, in this work, the downstream gyroradius is the same order of magnitude as the upstream gyroradius, $r_{\rm g} = 1.39r_{\rm g,u}$, where $r_{\rm g,u}$ is the upstream gyroradius in the upstream rest frame.

Figure 1. The x component of four velocity at the high-density clump, u_x, at $t = 2t_{\rm esc}$, as a function of the density of the clump, $n_{\rm cl}/n_0$. The triangles, squares, and circles show the results for the GSD approximation, the MHD simulation, and the PIC simulation, respectively.

further, as it propagates to the uniform downstream region. Since the velocity of the shocked clump in the downstream rest frame is nonrelativistic after the shock crossing, the temperature in the shocked clump is highly relativistic. Then, the momentum of the shocked clump in the downstream rest frame is approximately

$$P_{\rm cl} = \frac{4}{3}\Gamma M_{\rm cl}\gamma^2 v_{\rm cl,d}, \tag{1}$$

where $v_{\rm cl,d}$ and γ are the three velocity of the shocked clump and the corresponding Lorentz factor, respectively. The momentum flux that the clump sweeps is

$$F = (\epsilon + p)\gamma^2 \frac{v_{\rm cl,d}^2}{c^2}R_{\rm cl}^2, \tag{2}$$

where $\epsilon = 4\Gamma^2 n' m_{\rm p} c^2$ and p are the fluid energy density and pressure in the downstream uniform region, respectively, where $p \approx \epsilon/3$ for relativistically hot plasmas. $R_{\rm cl}^2$ is the cross section of the clump. $R_{\rm cl}$, n', and $m_{\rm p}$ are the comoving clump size, the comoving number density in the upstream uniform region, and the proton mass, respectively. Then, the deceleration time is given by

$$t_{\rm dec} = \frac{P_{\rm cl}}{F} = \frac{M_{\rm cl}}{\Gamma n' m_{\rm p} v_{\rm cl,d} R_{\rm cl}^2}. \tag{3}$$

In the above argument, we consider a clump in three-dimensional space. In two-dimensional space, as in our simulations, the cross section changes to $R_{\rm cl}$, but the relation of $t_{\rm dec} \propto \Gamma^{-1}$ does not change. We find that, in relativistic shocks, the deceleration time of the clump is Γ times shorter than that in nonrelativistic shocks. The fluid energy density ϵ in the downstream uniform region is a crucial factor for the rapid deceleration. The factor of Γ^2 originates from the Lorentz contraction concerning the number density and the random kinetic energy of each particle in the downstream region. Previous MHD simulations were performed in a mildly relativistic flow with an upstream bulk Lorentz factor of about 2. Thus, this effect has been neglected in previous studies.
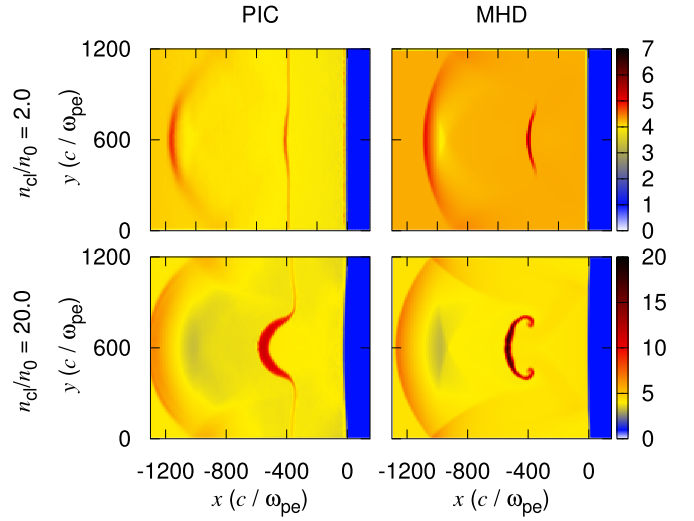

Figure 2. Density distribution, n/n_0, in the shock downstream region at $t = 2t_{\rm esc}$ for $n_{\rm cl}/n_0 = 2$ (top two panels) and $n_{\rm cl}/n_0 = 20$ (bottom two panels). The time, t, represents the elapsed time since the clump has interacted with the shock front. The left and right columns show the results for the PIC and MHD simulations, respectively. Movie: https://docs.google.com/presentation/d/ 1cseAc5ehoR-9V917zVC_lzvVw9Pi3a8Q/edit?usp=sharing&ouid=1123463 14884784410578&rtpof=true&sd=true.

In the PIC simulations, the clump velocity is decreased further. This is because the deceleration time in the PIC simulations is shorter than that in the MHD simulations, since the cross section of the clump becomes large due to the streaming of particles.

Figure 2 shows the density in the shock downstream region at $t = 2t_{\rm esc}$. The shock front is located at $x = 0$ and the left region ($x < 0$) is the shock downstream region. In the MHD simulation with $n_{\rm cl}/n_0 = 2$ (top right), the structure of the high-density clump is not significantly deformed by the downstream shear flow, even though the density of the clump is not so low. By inserting $M_{\rm cl} \approx n_{\rm cl}' R_{\rm cl}^3$ into Equation (3), the deceleration time is represented by

$$t_{\rm dec} = \frac{n_{\rm cl}'}{\Gamma n'}\frac{R_{\rm cl}}{v_{\rm cl,d}} = \frac{n_{\rm cl}'}{\Gamma n'}t_{\rm eddy}, \tag{4}$$

where $t_{\rm eddy} = R_{\rm cl}/v_{\rm cl,d}$ and $n_{\rm cl}'$ is the comoving number density of the upstream clump. For $n_{\rm cl}/n_0 = 2$, the deceleration time is shorter than the eddy turnover time ($t_{\rm dec} < t_{\rm eddy}$), so that the clump decelerates in the downstream region before the clump is deformed by the downstream shear flow. On the other hand, for $n_{\rm cl}/n_0 = 20$, the deceleration time is longer than the eddy turnover time ($t_{\rm dec} > t_{\rm eddy}$), so that the clump structure is strongly deformed. In the PIC simulations (the left two panels), the particles in the clump escape along the magnetic field line, because the particles get a large velocity dispersion after the shock heating. The density becomes almost uniform along the magnetic field line in the downstream region for $n_{\rm cl}/n_0 = 2$ (top left). In the PIC simulation with $n_{\rm cl}/n_0 = 20$ (bottom left), although the density is not completely uniform along the magnetic field line, the deformation of the clump structure is smaller than that in the MHD simulation. The high-density structures at $x = -1200c/\omega_{\rm pe}$ for all the cases are sound waves excited by the shock–clump interaction, which develop into a shock-like structure, due to the nonlinear steepening.
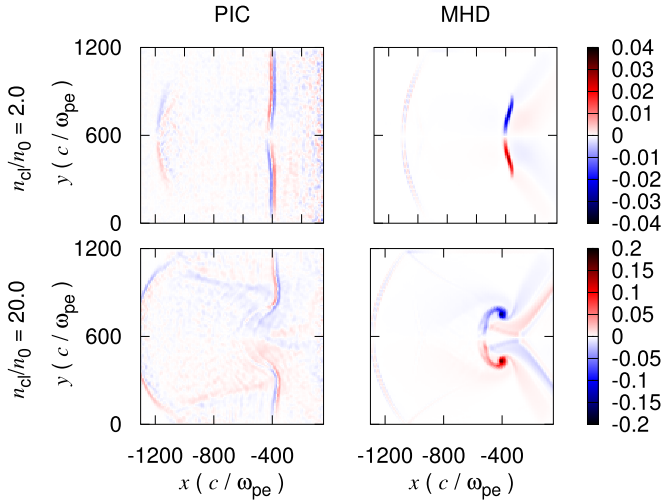
Figure 3. The same as Figure 2, but for the z component of vorticity, $(\vec{\nabla} \times \boldsymbol{u})_z$.

Figure 3 shows the z component of vorticity, $(\vec{\nabla} \times \boldsymbol{u})_z$, at $t = 2t_{esc}$. The vorticity in the PIC simulations (the left two panels) is significantly lower than that in the MHD simulations. As mentioned in Figure 1, the shocked clump decelerates more rapidly in the PIC simulations, because the particle streaming along the magnetic field line makes the cross section of the clump large. Since the vorticity is estimated by the clump velocity over the clump size, the vorticity is low for the PIC simulations.

The magnetic field strength, $|\boldsymbol{B}|$, at $t = 2t_{esc}$ is given in the left column in Figure 4. As expected from the vorticity shown in Figure 3, the magnetic field is strongly amplified by the vortex motion in the MHD simulation with $n_{cl}/n_0 = 20$, but not in the PIC simulations. The time evolution of the maximum strength of the downstream magnetic fields, B_{max}, is shown in Figure 5. Except for the PIC simulation with $n_{cl}/n_0 = 2$, the maximum field strength is at least three times larger than the shock compressed value of $4B_0$, i.e., $B_{max} \gtrsim 12B_0$. Moreover, the x component of the amplified field is comparable to or larger than $4B_0$ (see the right column in Figure 4), which is generated by the stretching of the magnetic field line. The shock compression and the downstream sound waves amplify only the y component of the magnetic field. Therefore, the growth of the magnetic field strength is due to the vortex motion. For $n_{cl}/n_0 = 2$, although the magnetic field continues to be amplified in the MHD simulations for a long time, it saturates at $t \sim 2t_{esc} = 1200\omega_{pe}^{-1}$ in the PIC simulation, where $B_{max} \sim 6B_0$. Since the saturation time is about $2t_{esc}$ in the PIC simulation with $n_{cl}/n_0 = 2$, the saturation of the magnetic field amplification originates from the particle escape. For a higher-density clump ($n_{cl}/n_0 = 20$), the magnetic field is amplified to the equipartition level with the upstream kinetic energy in the MHD simulation; that is, $B_{max} \sim B_0 \sqrt{\sigma_e}^{-1} \sim 31.6B_0$. On the other hand, in the PIC simulation, the growth rate is lower than that in the MHD simulation. Moreover, the magnetic field saturates before reaching the equipartition level. Therefore, our PIC simulations show that the downstream magnetic field is not efficiently amplified by the shock–clump interaction for relativistic collisionless shocks, even though the clump density is much higher than the mean density, $n_{cl}/n_0 = 20$.

To summarize the results, for the PIC simulations, the particle streaming motion causes a large velocity gradient scale, l, and a small velocity perturbation, δu. This leads to a very low vorticity around the shocked clump, $\delta u/l$, compared to that in the MHD simulations. This occurs even though the clump size is much larger than the gyroradius of the downstream particles. Therefore, the magnetic field amplification is slower or saturates at a lower level in the PIC simulations.

4. Discussion

We have considered a magnetized plasma with $\sigma_e = 10^{-3}$ in this work. For more weakly magnetized plasmas (lower σ_e), some kinetic plasma instabilities would be excited by the escape from the dense clump, which potentially generate magnetic field fluctuations (Tomita & Ohira 2016; Tomita et al. 2019). Such kinetic-scale magnetic field fluctuations could disturb the free-streaming motion along the magnetic field line. This could suppress the streaming escape along the magnetic field line. Even in collisionless systems, as long as the escape timescale due to diffusion or free streaming is longer than the eddy turnover time, the shock–clump interaction would drive the turbulent dynamo. On the other hand, the particle diffusion perpendicular to the magnetic field would occur in a realistic three-dimensional system (Jokipii et al. 1993; Giacalone & Jokipii 1994), so that it might be difficult to drive the turbulent dynamo by the shock–clump interaction. We will address the shock–clump interaction for more weakly magnetized colli-sionless shocks by means of three-dimensional PIC simulations in future work.

In our PIC simulations, the ratio of the clump size to the gyroradius of the downstream thermal electrons and positrons is $R_{cl}/r_g = 53.7$. In reality, the ratio of R_{cl}/r_g is widely distributed in laboratory, space, and astrophysical plasmas. Laboratory plasmas could have a similar value of $R_{cl}/r_g = \mathcal{O}(10)$–$\mathcal{O}(100)$, whereas it must be much larger than $\mathcal{O}(100)$ in astrophysical plasmas. The effects of escape and diffusion would depend on the ratio of R_{cl}/r_g. If the diffusion length scale is much smaller than the size of the clump, the particle streaming along the magnetic field does not occur, but the rapid deceleration due to the relativistic effect shown in our relativistic MHD simulation does occur. The diffusion length scale cannot be easily estimated, even in the simple system that we have considered. We need to conduct a parameter study for R_{cl}/r_g.

The clump structure in the downstream rest frame is likely important for driving the turbulent dynamo. Large-scale hybrid plasma simulations show that nonrelativistic collisionless shocks generate strong density fluctuations in the upstream region. These fluctuations result in the magnetic field amplification in the downstream, which may be interpreted as the shock–clump interactions (Caprioli & Spitkovsky 2013; Ohira 2016a, 2016b). For relativistic shocks, a spherical structure in the upstream rest frame is a structure compressed to the shock normal direction in the downstream rest frame, because of the the Lorentz contraction. Hence, the interaction time between the shock front and the dense clump is shorter, so that the velocity disturbance is smaller than that for nonrelativistic shocks. Furthermore, the compressed structure makes the deceleration time of the shocked clump short. Although the results are not shown here, we have confirmed with the PIC simulations that the magnetic field is amplified more efficiently by the interaction between a collisionless shock and a spherical clump in the shock down-stream frame. In addition, the particle streaming from a dense clump would be less important in nonrelativistic shocks, because the thermal velocity in the dense clump can be much slower than
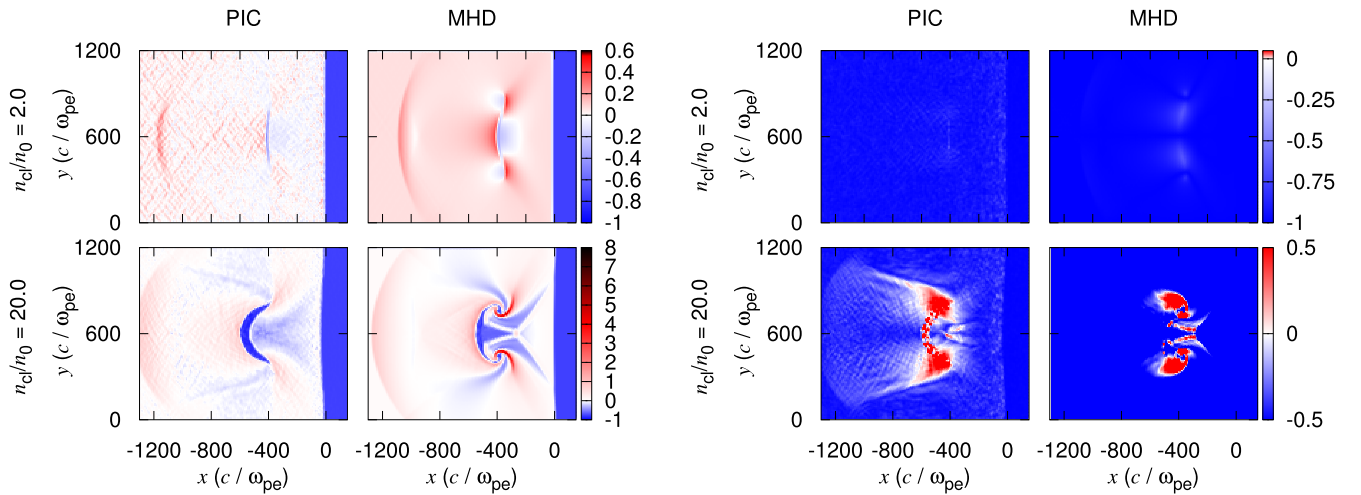
Figure 4. The same as Figure 2, but for the magnetic field strength $(B - 4B_0)/4B_0$ (left column) and the ratio of B_x to B_y, $|B_x/B_y| - 1$ (right column).
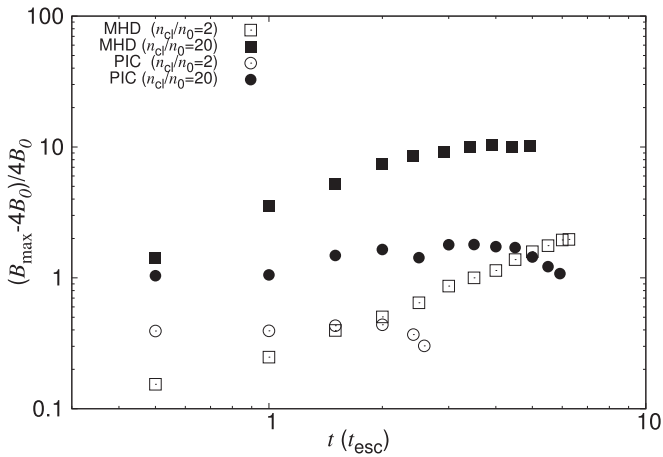
Figure 5. The time evolution of the maximum magnetic field amplification factor in the shock downstream region, $(B_{max} - 4B_0)/4B_0$. The time, t, represents the elapsed time since the clump has interacted with the shock front. The open and filled points show the results for $n_{cl}/n_0 = 2$ and 20, respectively. The squares and circles show the results for the MHD and PIC simulations, respectively.

the shock velocity for nonrelativistic shocks, but all velocity scales are always on the order of the speed of light for relativistic shocks. Therefore, relativistic shocks are not as suitable for the turbulent dynamo caused by the shock–clump interaction as nonrelativistic shocks.

The rapid deceleration of the shocked clump has been observed in both MHD and PIC simulations. The most kinetic energy of the clump is quickly converted to the energy of sound waves, which eventually evolve to weak shocks. Since shocks interact with multiple clumps in reality, the sound waves or weak shocks interact with each other, resulting in a strong turbulence in the downstream region (e.g., Inoue et al. 2011). Although such a nonlinear evolution has not been investigated in this work, we will perform larger PIC simulations in the future, to understand the turbulent dynamo in the collisionless shock propagating to a more realistic nonuniform medium. In addition to the turbulent dynamo, particle acceleration by downstream turbulence could be observed in that simulation (Ohira 2013; Pohl et al. 2015; Kimura et al. 2016; Zhdankin et al. 2018; Comisso & Sironi 2019; Kimura et al. 2019; Yokoyama & Ohira 2020).

5. Summary

In this work, we have performed the first PIC simulations of the shock–clump interaction in magnetized collisionless plasmas, finding that the downstream turbulence is significantly suppressed in collisionless shocks compared with the results of the MHD simulations, because particles escape from the dense clump region along the magnetic field line in the shock downstream region. As a result, the magnetic field is not strongly amplified by the turbulent dynamo, even though the upstream kinetic energy is much higher than that of the downstream magnetic field. Our simulation has demonstrated that the particle streaming or the diffusion have a significant impact on the dynamics at a length scale larger than the gyroradius. These processes cannot be handled by the MHD simulation. In addition, we have found that the dense clump quickly decelerates in the downstream regions of the relativistic shocks in the MHD and PIC simulations, because the clump structure is compressed in the shock normal direction by the Lorentz contraction. Thus, relativistic collisionless shocks are unsuitable for the downstream turbulent dynamo.

In many cases, we can only observe the emission from the shocked region. The spectra of the downstream magnetic field turbulence and accelerated particles are expected to depend on the upstream magnetization parameter and inhomogeneity. By conducting a parameter survey using large-scale PIC simulations, we will be able to obtain the dependence of the downstream spectra of the nonthermal particles and magnetic field strength on the upstream plasma condition. Combining the PIC simulation results and observations, we will be able to reveal the upstream plasma condition in the future. Therefore, large-scale kinetic simulations incorporating the inhomogeneity of ambient media open a new window to understanding laboratory, space, and astrophysical plasmas.

ORCID iDs

Sara Tomita ● https://orcid.org/0000-0001-7952-2474
Yutaka Ohira ● https://orcid.org/0000-0002-2387-0151
Shigeo S. Kimura ● https://orcid.org/0000-0003-2579-7266
Kengo Tomida ● https://orcid.org/0000-0001-8105-8113
Kenji Toma ● https://orcid.org/0000-0002-7114-6010

References

Abdalla, H., Adam, R., Aharonian, F., et al. 2019, Natur, 575, 464
Atzeni, S., & Meyer-ter-Vehn, J. 2004, The Physics of Inertial Fusion: Beam Plasma Interaction, Hydrodynamics, Hot Dense Matter (Oxford: Oxford Univ. Press)
Breuhaus, M., Reville, B., & Hinton, J. A. 2022, A&A, 660, A8
Caprioli, D., & Spitkovsky, A. 2013, ApJL, 765, L20
Comisso, L., & Sironi, L. 2019, ApJ, 886, 122
Fang, K., Kotera, K., & Olinto, A. V. 2012, ApJ, 750, 118
Fraschetti, F. 2013, ApJ, 770, 84
Giacalone, J., & Jokipii, J. R. 1994, ApJL, 430, L137
Giacalone, J., & Jokipii, J. R. 2007, ApJL, 663, L41
Godfrey, B. B. 1974, JCoPh, 15, 504
Heinze, J., Biehl, D., Fedynitch, A., et al. 2020, MNRAS, 498, 5990
Hennebelle, P., & Inutsuka, S.-I. 2019, FrASS, 6, 5
Ikeya, N., & Matsumoto, Y. 2015, PASJ, 67, 64
Inoue, T., Asano, K., & Ioka, K. 2011, ApJ, 734, 77
Inoue, T., Yamazaki, R., & Inutsuka, S.-i. 2009, ApJ, 695, 825
Iwamoto, M., Amano, T., Hoshino, M., et al. 2019, ApJL, 883, L35
Jokipii, J. R., Kota, J., & Giacalone, J. 1993, GeoRL, 20, 1759
Kakuwa, J., Toma, K., Asano, K., Kusunose, M., & Takahara, F. 2015, MNRAS, 449, 551
Kato, T. N. 2005, PhPl, 12, 080705
Keshet, U., Katz, B., Spitkovsky, A., & Waxman, E. 2009, ApJL, 693, L127
Kimura, S. S., Murase, K., & Zhang, B. T. 2018, PhRvD, 97, 023026
Kimura, S. S., Toma, K., Suzuki, T. K., & Inutsuka, S.-i. 2016, ApJ, 822, 88
Kimura, S. S., Tomida, K., & Murase, K. 2019, MNRAS, 485, 163
Kotera, K., & Olinto, A. V. 2011, ARA&A, 49, 119

Kumar, R., Eichler, D., & Gedalin, M. 2015, ApJ, 806, 165
Lhaaso Collaboration, Cao, Z., Aharonian, F., et al. 2021, Sci, 373, 425
Lucek, S. G., & Bell, A. R. 2000, MNRAS, 314, 65
MAGIC Collaboration, Acciari, V. A., Ansoldi, S., et al. 2019a, Natur, 575, 455
MAGIC Collaboration, Acciari, V. A., Ansoldi, S., et al. 2019b, Natur, 575, 459
Matsumoto, Y., Amano, T., & Hoshino, M. 2013, PhRvL, 111, 215003
Matsumoto, Y., Amano, T., Kato, T. N., & Hoshino, M. 2015, Sci, 347, 974
Mizuno, Y., Pohl, M., Niemiec, J., et al. 2011, ApJ, 726, 62
Mizuno, Y., Pohl, M., Niemiec, J., et al. 2014, MNRAS, 439, 3490
Murase, K., Dermer, C. D., Takami, H., & Migliori, G. 2012, ApJ, 749, 63
Niemiec, J., Ostrowski, M., & Pohl, M. 2006, ApJ, 650, 1020
Niemiec, J., Pohl, M., Bret, A., & Wieland, V. 2012, ApJ, 759, 73
Nishihara, K., Wouchuk, J. G., Matsuoka, C., Ishizaki, R., & Zhakhovsky, V. V. 2010, RSPTA, 368, 1769
Ohira, Y. 2013, ApJL, 767, L16
Ohira, Y. 2016a, ApJ, 817, 137
Ohira, Y. 2016b, ApJ, 827, 36
Ohira, Y., Terasawa, T., & Takahara, F. 2009, ApJL, 703, L59
Perkins, L. J., Ho, D. D. M., Logan, B. G., et al. 2017, PhPl, 24, 062708
Pohl, M., Wilhelm, A., & Telezhinsky, I. 2015, A&A, 574, A43
Sano, T., Inoue, T., & Nishihara, K. 2013, PhRvL, 111, 205001
Sano, T., Tamatani, S., Matsuo, K., et al. 2021, PhRvE, 104, 035206
Santana, R., Barniol Duran, R., & Kumar, P. 2014, ApJ, 785, 29
Shin, M.-S., Stone, J. M., & Snyder, G. F. 2008, ApJ, 680, 336
Sironi, L., & Goodman, J. 2007, ApJ, 671, 1858
Sironi, L., & Spitkovsky, A. 2012, CS&D, 5, 014014
Sironi, L., Spitkovsky, A., & Arons, J. 2013, ApJ, 771, 54
Spitkovsky, A. 2008a, ApJL, 682, L5
Spitkovsky, A. 2008b, ApJL, 673, L39
Stone, J. M., & Norman, M. L. 1992, ApJL, 390, L17
Stone, J. M., Tomida, K., White, C. J., & Felker, K. G. 2020, ApJS, 249, 4
Tanaka, S. J., & Takahara, F. 2011, ApJ, 741, 40
Tomita, S., & Ohira, Y. 2016, ApJ, 825, 103
Tomita, S., Ohira, Y., & Yamazaki, R. 2019, ApJ, 886, 54
Uchiyama, Y., Aharonian, F. A., Tanaka, T., Takahashi, T., & Maeda, Y. 2007, Natur, 449, 576
Weibel, E. S. 1959, PhRvL, 2, 83
White, C. J., Stone, J. M., & Gammie, C. F. 2016, ApJS, 225, 22
Yokoyama, S. L., & Ohira, Y. 2020, ApJ, 897, 50
Zhang, B. T., Murase, K., Kimura, S. S., Horiuchi, S., & Mészáros, P. 2018, PhRvD, 97, 083010
Zhdankin, V., Uzdensky, D. A., Werner, G. R., & Begelman, M. C. 2018, ApJL, 867, L18
Zhou, Y., Williams, R. J. R., Ramaprabhu, P., et al. 2021, PhyD, 423, 132838